Inorganic Chemistry
Cite This: Inorg. Chem. 2018, 57, 2260−2268
Article
pubs.acs.org/IC

Quaternary Pavonites $A_{1+x}Sn_{2-x}Bi_{5+x}S_{10}$ (A^+ = Li^+, Na^+): Site Occupancy Disorder Defines Electronic Structure

Jason F. Khoury,[†] Shiqiang Hao,[‡] Constantinos C. Stoumpos,[†] Zhenpeng Yao,[‡] Christos D. Malliakas,[†] Umut Aydemir,[§] Tyler J. Slade,[†] G. Jeffrey Snyder,[‡] Chris Wolverton,[‡] and Mercouri G. Kanatzidis*[,†]

[†]Department of Chemistry, Northwestern University, Evanston, Illinois 60208, United States
[‡]Department of Materials Science and Engineering, Northwestern University, Evanston, Illinois 60208, United States
[§]Department of Chemistry, Koc University, Sariyer, Istanbul 34450, Turkey

Supporting Information

ABSTRACT: The field of mineralogy represents an area of untapped potential for the synthetic chemist, as there are numerous structure types that can be utilized to form analogues of mineral structures with useful optoelectronic properties. In this work, we describe the synthesis and characterization of two novel quaternary sulfides $A_{1+x}Sn_{2-x}Bi_{5+x}S_{10}$ (A = Li^+, Na^+). Though not natural minerals themselves, both compounds adopt the pavonite structure, which crystallizes in the *C*2/*m* space group and consists of two connected, alternating defect rock-salt slabs of varying thicknesses to create a three-dimensional lattice. Despite their commonalities in structure, their crystallography is noticeably different, as both structures have a heavy degree of site occupancy disorder that affects the actual positions of the atoms. The differences in site occupancy alter their electronic structures, with band gap values of 0.31(2) eV and 0.07(2) eV for the lithium and sodium analogues, respectively. $LiSn_2Bi_5S_{10}$ exhibits ultralow thermal conductivity of 0.62 W m^{-1} K^{-1} at 723 K, and this result is corroborated by phonon dispersion calculations. This structure type is a promising host candidate for future thermoelectric materials investigation, as these materials have narrow band gaps and intrinsically low thermal conductivities.

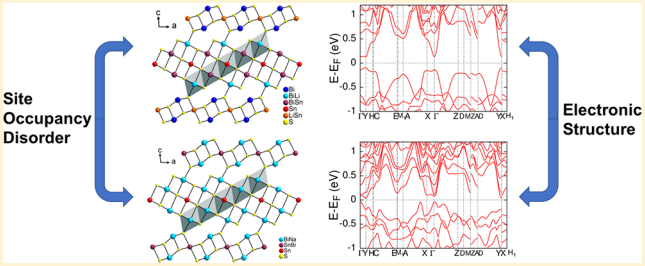

INTRODUCTION

Bismuth chalcogenides have garnered widespread interest, from semiconductors and thermoelectrics to superconductors, owing to their incredible diversity in electronic structure.[1,2] The layered narrow gap semiconductors $CsBi_4Te_6$ and $RbBi_{11/3}Te_6$ are superconducting at low T_c (4.4 and 3.2 K, respectively), which is remarkable considering that both compounds have low carrier densities that are not typically conducive to superconductive behavior.[2,3] Perhaps more importantly, many new bismuth chalcogenides with relatively complex structures can be predictably synthesized from canonical building blocks. The diversity and complexity in structure are greatly enhanced when group 14 elements such as Sn^{2+} and Pb^{2+} are added. These structures form several different homologous series with Bi_2Te_3-, CdI_2-, and NaCl-type subunits.[2,4] Further, expression of the stereoactive lone pair from the ns^2 orbital of Bi^{3+}, Sb^{3+}, Pb^{2+}, and Sn^{2+} allows for several unique coordination environments, such as capped octahedra, capped trigonal prisms, and trigonal bipyramids.[3,5] These unusual perturbations in local bonding can have broad implications on the crystal and electronic structures of extended solids featuring Bi^{3+}, Sb^{3+}, Pb^{2+}, and Sn^{2+}, resulting in a wide array of novel materials with emergent properties.[6]

Many of these materials are known for having considerable amounts of site occupancy disorder in several naturally occurring sulfosalts, as long as the other metal can adapt a similar coordination environment.[7,8] Incredibly, bismuth (and other similarly sized elements, such as antimony, tin, and lead) can also have mixed occupancy with alkali metals of considerably smaller ionic radii so long as they can adapt the same coordination environment, as in the case of $LiBi_3S_5$[9] and $LiPbSb_3S_6$.[10] As a result of these phenomena, there have been a considerable wealth of synthetic sulfosalts and selenosalts that have significant site occupancy disorder, the effect of which on their electronic properties has not been thoroughly investigated.[11−13]

Pavonite ($AgBi_3S_5$) is a naturally occurring sulfosalt that has shown promise as a thermoelectric material due to its extremely low thermal conductivity and good electrical properties.[14] Pavonite is a three-dimensional structure with a layered rock-salt motif containing two distinct slabs. The first, thicker PbS-type slab consists of BiS_6 octahedra oriented as diagonal chains, and these chains are flanked by the thinner SnSe-type slabs consisting of AgS_6 octahedra surrounded by BiS_5 square pyramids.[14] The structure pavonite is part of the homologous series $M'_{n+1}Bi_2Q_{n+5}$, where the M′ cations can be bismuth, alkali metal, lead, silver, or copper, and the Q anions are sulfur,

Received: December 13, 2017
Published: February 7, 2018

DOI: 10.1021/acs.inorgchem.7b03091
Inorg. Chem. 2018, 57, 2260−2268

Table 1. Crystal Data and Structure Refinement for $LiSn_2Bi_5S_{10}$ and $NaSn_2Bi_5S_{10}$ at 298 K

empirical formula	$Li_{0.97(3)}Sn_{2.06(2)}Bi_{4.97(2)}S_{10(0)}$ [a]	$Na_{1.04(2)}Sn_{1.84(0)}Bi_{5.11(3)}S_{10(0)}$ [b]
formula weight	1609.90	1631.95
temperature	298 K	298 K
wavelength	0.71073 Å	0.71073 Å
crystal system	monoclinic	monoclinic
space group	$C2/m$	$C2/m$
unit cell dimensions	a = 13.148(3) Å, α = 90°	a = 13.311(3) Å, α = 90°
	b = 4.0186(8) Å, β = 93.93(3)°	b = 4.0470(8) Å, β = 93.64(3)°
	c = 16.607(3) Å, γ = 90°	c = 16.794(3) Å, γ = 90°
volume	875.4(3) Å^3	902.8(3) Å^3
Z	2	2
density (calculated)	6.108 g/cm^3	6.003 g/cm^3
absorption coefficient	53.820 mm^{-1}	53.326 mm^{-1}
F(000)	1356	1376
crystal size	0.1745 × 0.1049 × 0.0112 mm^3	0.0964 × 0.0531 × 0.0164 mm^3
θ range for data collection	2.459 to 29.207°	2.430 to 25.974°
index ranges	$-18 \le h \le 16$, $-5 \le k \le 5$, $-22 \le l \le 22$	$-16 \le h \le 16$, $-4 \le k \le 4$, $-18 \le l \le 20$
reflections collected	4242	3187
independent reflections	1349 [R_{int} = 0.0434]	1008 [R_{int} = 0.0649]
completeness to θ = 26.000°, 25.974°	99.7%	99.9%
refinement method	full-matrix least-squares on F^2	full-matrix least-squares on F^2
data/restraints/parameters	1349/0/61	1008/0/60
goodness-of-fit	1.090	1.279
final R indices [$I > 2\sigma(I)$]	R_{obs} = 0.0390, wR_{obs} = 0.0932	R_{obs} = 0.0675, wR_{obs} = 0.1661
R indices [all data]	R_{all} = 0.0490, wR_{all} = 0.0972	R_{all} = 0.0814, wR_{all} = 0.1710
extinction coefficient	0.00084(11)	N/A
largest diff peak and hole	1.717 and −1.585 e·Å^{-3}	2.945 and −5.082 e·Å^{-3}

[a] $Li_{0.97(3)}Sn_{2.06(2)}Bi_{4.97(2)}S_{10(0)}$: $R = \sum||F_o| - |F_c||/\sum|F_o|$, $wR = \{\sum[w(|F_o|^2 - |F_c|^2)^2]/\sum[w(|F_o|^4)]\}^{1/2}$ and $w = 1/[\sigma^2(F_o^2) + (0.0557P)^2 + 4.8554P]$ where $P = (F_o^2 + 2F_c^2)/3$. [b] $Na_{1.04(2)}Sn_{1.84(0)}Bi_{5.11(3)}S_{10(0)}$: $R = \sum||F_o| - |F_c||/\sum|F_o|$, $wR = \{\sum[w(|F_o|^2 - |F_c|^2)^2]/\sum[w(|F_o|^4)]\}^{1/2}$ and $w = 1/[\sigma^2(F_o^2) + (0.0523P)^2 + 238.6890P]$ where $P = (F_o^2 + 2F_c^2)/3$.

selenium, or tellurium.. The original pavonite mineral is the n = 5 member of this homologous series.

For $AgBi_3S_5$, it has been proposed that its low thermal conductivity is the result of a "double rattling" mechanism with the phonon modes of the Ag and Bi atoms in the structure, causing a phonon dampening effect that reduces lattice thermal conductivity of the material.[15] The double rattling mechanism is where both Ag and Bi atoms have two peaks in the partial density of states as a function of frequency, suggesting that both atoms are responsible for suppressing the lattice thermal conductivity of $AgBi_3S_5$. This mechanism is distinct from the concerted rattling effect in $CsAg_5Te_3$, where the Ag sublattice atoms all oscillate in the same phase and only one broad peak in the partial density of states is observed.[16] Rattling effects in materials with complex crystal structures allow for an additional method of scattering acoustic phonons without sacrificing performance in their electrical properties, therefore making them attractive candidates for thermoelectric materials.

In this work, we describe the synthesis, crystal structure, and characterization of two novel quaternary bismuth chalcogenides $ASn_2Bi_5S_{10}$ ($A = Li^+$, Na^+) with the n = 5 pavonite structure. Although both compounds have the same structure type, their differences in site occupancy disorder cause noticeable changes in their electronic structures and optical properties. Electrical measurements on $LiSn_2Bi_5S_{10}$ show that it behaves like a doped n-type semiconductor with a conductivity of 165 S/cm and carrier concentration of 1.21×10^{19} cm^{-3} at room temperature. $LiSn_2Bi_5S_{10}$ has ultralow thermal conductivity of 0.625 W m^{-1} K^{-1} at 723 K, which is lower than that of synthetic pavonite at the same temperature, likely due to its considerable site occupancy disorder. Phonon dispersion calculations are used to create simulated lattice thermal conductivity of $LiSn_2Bi_5S_{10}$, with the simulated values being much higher than the actual values, likely due to the significant site occupancy disorder and minor impurity phase of the experimental compound.

EXPERIMENTAL SECTION

Reagents. All chemicals in this study were used as obtained: bismuth metal (99.9%, Strem Chemicals, Inc., Newburyport, MA), sulfur pieces (99.998%, Sigma-Aldrich, St. Louis, MO), tin chunks (99.999%, American Elements, Los Angeles, CA), lithium metal rods (99.9%, 12.7 mm diameter, Sigma-Aldrich, St. Louis, MO), and sodium metal (99.95%, Sigma-Aldrich, St. Louis, MO). Li_2S and Na_2S were synthesized from stoichiometric amounts of the constituent elements reacted in liquid ammonia, as described in the Supporting Information.

Synthesis. *$LiSn_2Bi_5S_{10}$.* Li_2S (0.2529 g, 5.504 mmol), Sn (1.2594 g, 10.609 mmol), Bi (6.6250 g, 31.702 mmol), and S (1.8620 g, 58.079 mmol) were loaded in a 13 mm carbon coated silica tube in a dry, nitrogen glovebox. The tube was flame-sealed under vacuum at approximately 2×10^{-3} mbar, heated to 800 °C in 8 h, held there for 2 h, and water quenched to room temperature. This compound was then sealed in a second 13 mm carbon coated fused silica tube, heated to 800 °C in 24 h, held there for 2 h, and cooled to room temperature in 48 h. The above 1:1:3:6 molar ratio of Li:Sn:Bi:S with this process resulted in a bulk pure material, but the original 1:2:5:10 ratio had minor impurities. This excess of lithium accounts for glass attack with the tube, and the deficiency of tin is most likely the result of the bulk material being tin deficient compared to the ideal stoichiometry. Bulk pure $LiSn_2Bi_5S_{10}$ was synthesized by this process, and crystals suitable for single crystal diffraction were obtained by breaking up the ingot. The reaction produced the product in quantitative yield and is stable in open air at room temperature.

DOI: 10.1021/acs.inorgchem.7b03091
Inorg. Chem. 2018, 57, 2260−2268

$NaSn_2Bi_5S_{10}$. Na_2S (0.2600 g, 3.331 mmol), Sn (1.4602 g, 12.301 mmol), Bi (6.4264 g, 30.751 mmol), and S (1.8735 g, 58.428 mmol) were loaded in a 13 mm carbon coated fused silica tube in a dry, nitrogen glovebox. Na_2S had a 10% molar excess to account for glass attack with the silica tube. The tube was flame-sealed under vacuum at approximately 2×10^{-3} mbar, heated to 800 °C in 8 h, held there for 2 h, and water quenched to room temperature. The reaction produced the product in quantitative yield with minor impurities present in the powder X-ray diffraction pattern, and is stable in open air at room temperature.

Powder X-ray Diffraction. Powder X-ray diffraction (PXRD) patterns were taken using a Rigaku Miniflex powder X-ray diffractometer with Ni-filtered Cu Kα radiation (λ = 1.5406 Å) with a 30 kV voltage and 15 mA current. The diffraction pattern had a scan width of 0.02° and a scan rate of 10°/min. Simulated PXRD patterns were created using the software Mercury. Synchrotron X-ray diffraction was measured on $LiSn_2Bi_5S_{10}$ using the high-resolution diffractometer 11BM-B at the Advanced Photon Source of Argonne National Laboratory. The synchrotron sample was measured at 295 K with a nominal 2θ step size of 0.001° and a scan rate of 0.1 step/s. The wavelength of synchrotron radiation was λ = 0.412642 Å.

Single Crystal X-ray Diffraction. An IPDS 2T single crystal X-ray diffractometer, running at 50 kV and 40 mA with Mo Kα radiation (λ = 0.71073 Å), was used to gather data on the crystal structures of $LiSn_2Bi_5S_{10}$ and $NaSn_2Bi_5S_{10}$. Single crystals of both compounds were adhered to a glass fiber with super glue, and all data were collected at room temperature. The data were collected, analyzed, and integrated using the X-AREA[17] software, where X-RED integrated the data and X-SHAPE applied the numerical absorption correction based on the crystal's shape and composition. The data was solved with SHELXT using Direct Methods, and refined with SHELXL using the Least Squares method.[18] The crystallographic information for both structures can be found in Tables 1–3. Additional crystallographic information can be found in the Supporting Information.

Table 2. Bond Lengths [Å] for $LiSn_2Bi_5S_{10}$ at 293(2) K with Estimated Standard Deviations in Parentheses

label	distances
Bi(1)–S(1)	2.582(4)
Bi(1)–S(3)	2.774(2)
Bi(2)/Li(1)–S(3)	2.642(4)
Bi(2)/Li(1)–S(5)	2.745(2)
Bi(3)/Sn(1)–S(2)	2.878(3)
Bi(3)/Sn(1)–S(4)	2.780(3)
Bi(3)/Sn(1)–S(5)	2.665(3)
Sn(2)–S(2)	2.825(2)
Sn(3)–S(1)	2.825(2)
Sn(3)–S(3)	2.479(4)

Table 3. Bond Lengths [Å] for $NaSn_2Bi_5S_{10}$ at 293(2) K with Estimated Standard Deviations in Parentheses

label	distances
Bi(1)/Na(1)–S(1)	2.882(7)
Bi(1)/Na(1)–S(4)	2.800(8)
Bi(1)/Na(1)–S(5)	2.678(11)
Bi(2)/Na(2)–S(1)	2.952(10)
Bi(2)/Na(2)–S(3)	2.685(10)
Bi(2)/Na(2)–S(5)	2.761(7)
Bi(3)/Na(3)–S(2)	2.644(11)
Bi(3)/Na(3)–S(3)	2.757(7)
Sn(1)/Bi(4)–S(2)	2.855(7)
Sn(1)/Bi(4)–S(3)	2.733(12)
Sn(2)–S(4)	2.914(15)

Scanning Electron Microscopy and Energy Dispersive Spectroscopy (EDS). Images and quantitative analysis (apart from lithium) were performed with a Hitachi S-3400 scanning electron microscope that was equipped with a PGT energy-dispersive X-ray analysis instrument. Lithium cannot be detected by EDS due to its low electron count, so the results of $LiSn_2Bi_5S_{10}$ do not have lithium in the atomic percentages. To account for this, X-ray photoelectron spectroscopy (XPS) and inductively coupled plasma optical emission spectroscopy (ICP-OES) were used to confirm the presence of lithium in the structure. EDS was performed at 25 kV, 70 mA probe current, and a 60 s acquisition time. The chemical compositions of each crystal were the result of averaged compositions from multiple single-point data collections.

Differential Thermal Analysis (DTA). Differential thermal analysis (DTA) was performed using a Netzsch STA 449 F3 Jupiter simultaneous thermal analysis (STA) instrument. The samples were ground to a fine powder, loaded into carbon-coated silica ampules (approximately 40 mg in each ampule), and flame-sealed under vacuum. Each sample was compared to a sealed silica ampule containing aluminum oxide (Al_2O_3) of comparable mass. Each sample was heated to 800 °C at a rate of 10 °C/min, held at 800 °C for 5 min, and cooled back down at a rate of 10 °C/min. Each sample went through two cycles to show that the behavior was repeatable. After DTA was performed, a PXRD of each compound (see Supporting Information) was taken to determine if they melted congruently.

Fourier-Transform Infrared Spectroscopy (FTIR). Fourier-transform infrared spectroscopy (FTIR) was performed using a Nicolet 6700 IR spectrometer under constant flow of nitrogen with a diffuse reflectance setup (Figure 4). A metal mirror was used as a 100% reflectance standard that all of the spectra were compared to. Absorbance (α/S) data were calculated from the FTIR reflectance data using the Kubelka–Munk equation ($\alpha/S = (1 - R^2)/2R$), where α is the absorption coefficient, S is the scattering coefficient, and R is reflectance.[19] The band gap of the material was estimated by using a linear fit of the absorption edge.

Density Functional Theory (DFT) Calculations. The total energies and relaxed geometries were calculated by DFT within the generalized gradient approximation (GGA) of Perdew–Burke–Ernzerhof, the exchange correlation functional with Projector Augmented Wave potentials.[20] We use periodic boundary conditions and a plane wave basis set as implemented in the Vienna ab initio simulation package.[21] The total energies were numerically converged to approximately 3 meV/cation using a basis set energy cutoff of 500 eV and dense k-meshes corresponding to 4000 k-points per reciprocal atom in the Brillouin zone.

To do a DFT band structure calculation for a material with experimentally determined mixed occupancy of the individual sites, we first identified the lowest energy configuration of $LiSn_2Bi_5S_{10}$ and $NaSn_2Bi_5S_{10}$ from many geometrically distinct Bi/Li(Na)/Sn possibilities. In simpler terms, we enumerate all structural possibilities within a 72-atom cell and rank their electrostatic energies. For the 10 structures with the lowest electrostatic energies, we perform further DFT calculations to determine the most favorable (lowest energy) structure. The details of searching for the most favorable structures have been applied to other materials and are described in Supporting Information.[22] After implementing this strategy, we that found the ground state structures of $LiSn_2Bi_5S_{10}$ and $NaSn_2Bi_5S_{10}$ are quite different even though the two materials have the same composition.

Phonon Dispersion Calculations. To quantitatively explore the origin of very low lattice thermal conductivity at the atomic level, we employed the Debye–Callaway model to quantitatively evaluate the lattice thermal conductivity of $LiSn_2Bi_5S_{10}$. It is known that the Grüneisen parameters, which characterize the relationship between phonon frequency and crystal volume change, allow us to estimate the lattice anharmonicity and better understand the physical nature of lattice thermal conductivity. The phonon and Grüneisen dispersions are calculated using first-principles DFT phonon calculations within the quasi-harmonic approximation. The $LiSn_2Bi_5S_{10}$ phonon dispersions are calculated on a 108 atom cell at two volumes: one is the

DOI: 10.1021/acs.inorgchem.7b03091
Inorg. Chem. 2018, 57, 2260–2268

equilibrium volume V_0, and another one is the isotropically compressed volume $0.98V_0$.

The Debye−Callaway formalism[23] has been shown to produce accurate values of lattice thermal conductivity, compared to experiment, for low-conductivity thermoelectric compounds.[24] The total lattice thermal conductivity can be written as a sum over one longitudinal κ_{LA} and two transverse κ_{TA} and $\kappa_{TA'}$ acoustic phonon branches: $\kappa_{Latt} = \kappa_{LA} + \kappa_{TA} + \kappa_{TA'}$. The partial conductivities κ_i (i corresponds to TA, TA′, and LA modes) are given by

$$\kappa_i = \frac{1}{3} C_i T^3 \left\{ \int_0^{\Theta_i/T} \frac{\tau_c^i(x) x^4 e^x}{(e^x - 1)^2} dx + \frac{\left[\int_0^{\Theta_i/T} \frac{\tau_c^i(x) x^4 e^x}{\tau_N^i (e^x - 1)^2} dx \right]^2}{\int_0^{\Theta_i/T} \frac{\tau_c^i(x) x^4 e^x}{\tau_N^i \tau_U^i (e^x - 1)^2} dx} \right\} \quad (1)$$

In this expression, Θ_i is the longitudinal (transverse) Debye temperature, $1/\tau_N^i$ is the scattering rate for normal phonon processes, $1/\tau_R^i$ is the sum of all resistive scattering processes, and $1/\tau_c^i = 1/\tau_N^i + 1/\tau_R^i$, $x = \hbar\omega/k_B T$, and $C_i = k_B{}^4/2\pi^2\hbar^3 v_i$, here, $\hbar$ is the Planck constant, k_B is the Boltzmann constant, ω is the phonon frequency, and v_i is the longitudinal or transverse acoustic phonon velocity.

The resistive scattering rate is the sum of scattering rates due to Umklapp phonon−phonon scattering ($1/\tau_U^i$), mass-difference impurity scattering ($1/\tau_m^i$), boundary scattering ($1/\tau_B^i$), and electron−phonon scattering ($1/\tau_{e-ph}^i$). In the pure single crystal compounds considered here, we ignore the effect of impurity scattering, and we assume that boundary and electron−phonon scattering contributions can be ignored at temperatures above approximately 100 K. Thus, the resistive scattering rate is mainly determined by the Umklapp phonon−phonon processes ($1/\tau_R^i \cong 1/\tau_U^i$). The normal phonon scattering and Umklapp can be written as

$$\frac{1}{\tau_N^{LA}(x)} = \frac{k_B{}^5 \gamma_{LA}{}^2 V}{M\hbar^4 v_{LA}{}^5} x^2 T^5 \quad (2)$$

$$\frac{1}{\tau_N^{TA/TA'}(x)} = \frac{k_B{}^5 \gamma_{TA/TA'}{}^2 V}{M\hbar^4 v_{TA/TA'}{}^5} x T^5 \quad (3)$$

$$\frac{1}{\tau_U^i(x)} = \frac{k_B{}^2 \gamma_i^2}{M\hbar v_i{}^2 \Theta_i} x^2 T^3 e^{-\theta_i/3T} \quad (4)$$

where γ, V, and M are the Gruneisen parameter, the volume per atom, and the average mass of an atom in the crystal, respectively. The Grüneisen parameter can be defined as $\gamma_i = -\frac{V\partial\omega_i}{\omega_i \partial V}$, characterizing the relationship between phonon frequency and volume change.

Inductively Coupled Plasma Optical Emission Spectroscopy (ICP-OES). ICP-OES measurements to detect the presence of lithium and approximate the molar ratios for $LiSn_2Bi_5S_{10}$ were conducted using a Thermo iCap 7600 ICP-OES instrument. $LiSn_2Bi_5S_{10}$ (5 mg) was dissolved in 0.6 mL of aqua regia, and then diluted to a 10 mL sample with a 3% (by weight) HNO_3 solution. All standards and blank samples were also diluted with the same 3% HNO_3 solution. Due to the evolution of H_2S gas upon dissolving the compound in aqua regia, the amount of sulfur was not measured when performing the experiment.

Spark Plasma Sintering (SPS). Ingots of both compounds were ground into fine powders and sieved (53 μm) to ensure small and homogeneous particle sizes. These powders were then loaded into 12.7 mm graphite dies, and spark plasma sintering (SPS) with an SPS-211LX, Fuji Electronic Industrial Co. Ltd., instrument was performed to turn them into dense ingots suitable for cutting and polishing for thermoelectric measurements. The sample was placed under vacuum and 40 MPa of pressure, while the heating profile was elevated to 500 °C in 5 min, held there for another 5 min, and then cooled to room temperature with the sintering turned off. The ingots created from SPS achieved approximately 93% of the theoretical density of each compound.

Electrical Conductivity and Seebeck Measurements. Electrical conductivity and Seebeck coefficient measurements were obtained using an ULVAC Riko ZEM-3 instrument under a low-pressure helium atmosphere from room temperature to 600 °C. The sample was cut perpendicular to SPS pressure with approximate dimensions of 3.5 × 3.5 × 10 mm^3, and were coated with a thin layer of boron nitride on all sides except the points of electrical contact to minimize melting during the measurement. The electrical conductivity measurement had an uncertainty of about 10%.[25]

Hall Effect and Carrier Concentration Measurements. Room temperature Hall coefficient and carrier concentration of $LiSn_2Bi_5S_{10}$ were measured on an SPS-obtained pellet (thickness <2 mm) using the van der Pauw technique under a magnetic field of 2 T using pressure-assisted tungsten electrodes.[25] Room temperature electrical resistivity was also measured. See Supporting Information for additional details.

Thermal Conductivity Measurements. Samples for thermal conductivity measurements were cut from the same sintered ingot used for the electrical measurements, and measured on a Netzsch Laser Flash Analysis (LFA) 457 setup. The samples were cut perpendicular to SPS pressure with dimensions of 6.0 × 6.0 × 2.0 mm^3, and were coated with a thin layer of graphite to prevent any light emission from the sample during the measurement. The samples were measured from room temperature up to 600 °C, and were under the presence of a persistent nitrogen atmosphere. The density for each sintered material was approximately 93% of the theoretical value, and the heat capacity was estimated with the Dulong−Petit law, where $C_p = 3R/\bar{M}$ (R is the ideal gas constant, and $\bar{M}$ is the average molar mass of each material). The total thermal conductivity was calculated to be $\kappa_{tot} = DC_pd$, where D is diffusivity, C_p is estimated heat capacity, and d is the experimental density value. These data were analyzed by the Cowan model as reported previously[25] (with pulse correction included), and the uncertainty is approximately 8%.

RESULTS AND DISCUSSION

Synthesis and Purification. Although we expected $LiSn_2Bi_5S_{10}$ to form by stoichiometric combination of the elements, the ratio of the starting materials was 1:1:3:6 for Li:Sn:Bi:S. This ratio implies that the melt is rich in lithium, but tin deficient, with bismuth and sulfur being accommodated correctly. Interestingly, the in-house obtained PXRD pattern did not show noticeable impurities or an amorphous background. This off-stoichiometric ratio is partially attributable to some of the lithium reacting with the fused silica tube in the melt despite the presence of carbon coating, requiring extra reagent to ensure a stoichiometric ratio. To investigate this further, we carried out synchrotron powder X-ray diffraction on $LiSn_2Bi_5S_{10}$ to examine impurities below the threshold of the Rigaku Miniflex (Figure 1). The results can be seen in Figure 2, as there is a minor secondary phase that has been fitted via LeBail refinement of the synchrotron pattern. The lattice parameters of the secondary phase suggest that it is an $n = 4$ pavonite in the Li−Sn−Bi−S homologous series, as the c parameter is smaller and the β angle is coincident with previously reported $n = 4$ pavonite compounds.[26] Due to the complicated nature of these structures, precise quantitation of the secondary phase as well as precise identification of its stoichiometry cannot be determined.

The ICP-OES elemental analysis data (see Supporting Information) show a larger molar amount of tin compared to lithium (1.12:1 ratio for Sn:Li) in the product. The Bi:Sn ratio in the product is also 2.78:1, slightly less than the experimental molar ratio of 3:1. Energy dispersive X-ray spectroscopy (EDS) confirmed a 2:1 ratio of S:Bi (see Supporting Information), as ICP-OES cannot adequately detect sulfur due to dissolution as H_2S when dissolving the compound in aqua regia. These data

DOI: 10.1021/acs.inorgchem.7b03091
Inorg. Chem. 2018, 57, 2260−2268

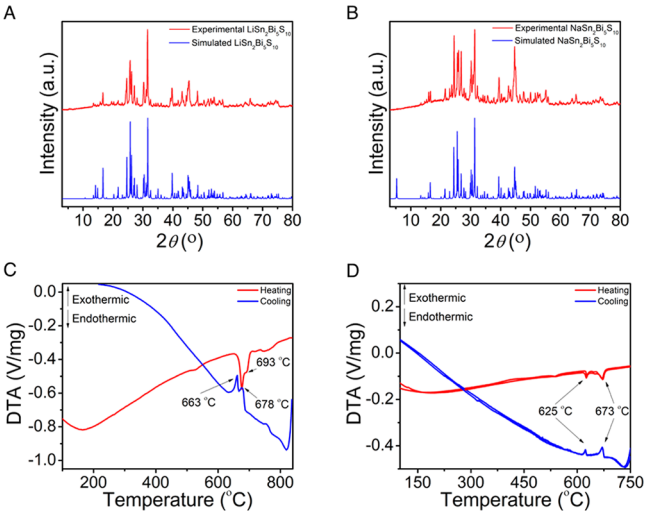

Figure 1. Powder X-ray diffraction patterns (Cu Kα radiation, λ = 1.5406 Å) and differential thermal analysis (DTA) graphs of $LiSn_2Bi_5S_{10}$ (A and C, respectively) and $NaSn_2Bi_5S_{10}$ (B and D, respectively). There is a shoulder melting event in B at 693 °C, but no secondary phase in the PXRD pattern, suggesting the presence of a high temperature precipitate redissovled into the matrix. The metastable phase $NaSn_2Bi_5S_{10}$ also has a minor secondary phase that melts at 625 °C.

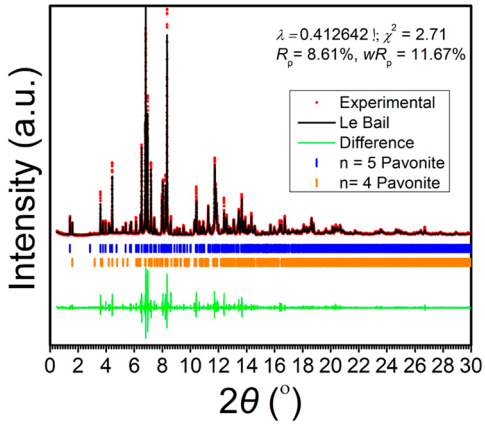

Figure 2. Synchrotron X-ray diffraction (SXRD, λ = 0.412642 Å) and LeBail fit of $LiSn_2Bi_5S_{10}$. The fit suggests that the lithium-rich secondary phase is an n = 4 pavonite, as the lattice parameters of the secondary phase are a = 13.1933(2) Å, b = 4.02963(6) Å, c = 15.0152(2) Å, β = 99.233(1)°.

suggest that there is an excess of lithium in the sample, and this can be explained by the presence of a lithium-rich secondary phase that can only be detected with synchrotron X-ray diffraction.

The DTA of this compound shows a dominant melting event at 677 °C and a shoulder melting event at approximately 690 °C, with matching crystallization events at 661 and 677 °C. The dominant melting event and its shoulder correspond to the primary phase $LiSn_2Bi_5S_{10}$ and the secondary n = 4 pavonite phase, respectively. The fact that the melting points of the two phases are so close together further suggests that they are in the same homology, as different n-members of homologous series tend to have incremental changes in their physical properties.[6]

$NaSn_2Bi_5S_{10}$ was synthesized at the nominal 1:2:5:10 molar ratio of Na:Sn:Bi:S, and the PXRD showed the presence of the intended major pavonite phase along with a minor secondary phase $Sn_{0.22}Bi_{1.78}S_{2.88}$.[27] The DTA showed melting events at 673 and 625 °C for the major and minor phases, respectively, with crystallization events at approximately the same temperatures for each. The compound could not be sintered into a pellet for thermoelectric measurements, as the structure decomposes when it is annealed. This indicates that $NaSn_2Bi_5S_{10}$ is a kinetic phase that is only isolable via quenching from the melt, whereas $LiSn_2Bi_5S_{10}$ is a more robust, thermodynamic phase.

Structure Description. $LiSn_2Bi_5S_{10}$ and $NaSn_2Bi_5S_{10}$ were determined to have the pavonite structure type, which consists of two alternating rock-salt (either PbS- or SnSe-type) slabs that were cut perpendicular to the [311] direction of the cubic rock-salt lattice. (See Figure 3.) The three-dimensional

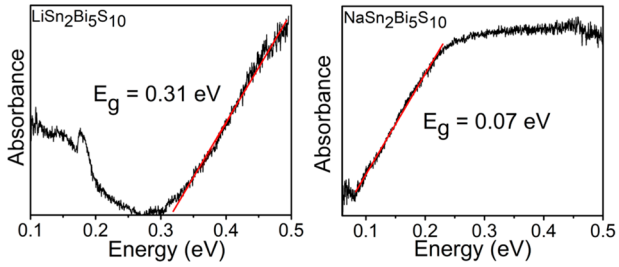

Figure 4. FTIR diffuse reflectance data for $LiSn_2Bi_5S_{10}$ (left) and $NaSn_2Bi_5S_{10}$ (right), with measured band gaps of 0.31(2) and 0.07(2) eV, respectively.

structure is anisotropic and part of the homologous series $M'_{n+1}Bi_2Q_{n+5}$, where the M′ cations can be bismuth, alkali metal, lead, silver, or copper, and the Q anions are sulfur or

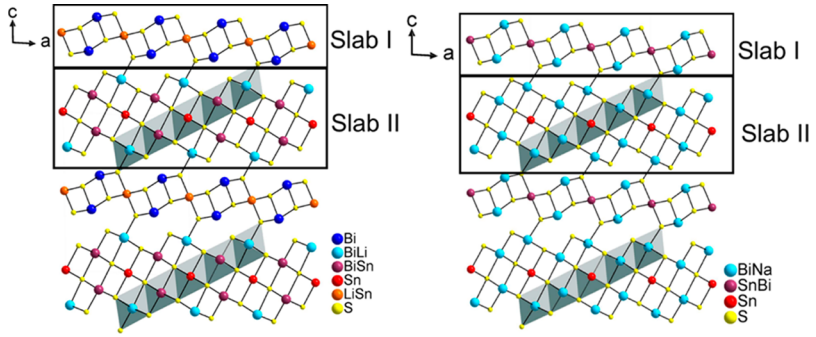

Figure 3. Crystal structures of $LiSn_2Bi_5S_{10}$ (left) and $NaSn_2Bi_5S_{10}$ (right). Both contain the same motif of pseudolayered alternating rock-salt slabs, but the right structure is notable in how the alkali metal is distributed across the bismuth sites.

DOI: 10.1021/acs.inorgchem.7b03091
Inorg. Chem. 2018, 57, 2260−2268

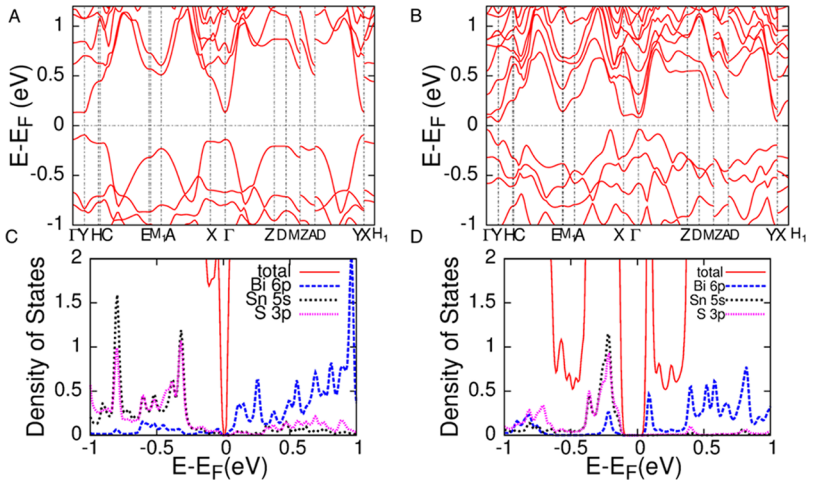

Figure 5. (A, B) Electronic band structures for $LiSn_2Bi_5S_{10}$ and $NaSn_2Bi_5S_{10}$ respectively. The Fermi level is at 0 eV in both graphs. (C, D) Partial and full density of states for $LiSn_2Bi_5S_{10}$ and $NaSn_2Bi_5S_{10}$ respectively. The alkali metal is not included due to minimal contribution to either the VBM or CBM of each structure.

selenium. The naturally occurring pavonite mineral, $AgBi_3S_5$, along with the two compounds described in this work, are the n = 5 member of this homologous series. In this structure type, the thinner slab (Slab I) is invariant to changes in the n-member and consists of $[M'S_6]$ octahedra flanked by two $[BiS_5]$ square pyramids, forming SnSe-type layers along the [010] direction. The thicker slab (Slab II) is a distorted PbS-type structure fragment, incorporated in pavonite along the [111] direction. The number of face-sharing octahedra in a diagonal chain is equal to the number of the n-member.[28]

For $LiSn_2Bi_5S_{10}$, Slab I is unique in that the M′ in the $M'S_6$ octahedron is a site of mixed occupancy, where it is a $[LiS_6]$ octahedron in 72% of unit cells and a $[SnS_6]$ octahedron in the other 28%, and the surrounding coordination environments are the same $[BiS_5]$ square pyramids that are common for this structure. While it is remarkable that ions of such differing sizes as Li^+ and Sn^{2+} (0.76 and 1.18 Å, respectively) can occupy the same site, there is precedence for this phenomenon in other disordered pavonite structures containing lithium.[9] The shorter bond lengths are also evidence of mixed occupancy, as the unique bonds at the mixed site (2.479(4) Å and 2.825(2) Å) are on average shorter than that of the unmixed $[SnS_6]$ site (2.825(2) Å and 2.888(4) Å) in the structure. The large asymmetry of the $[(Li/Sn)S_6]$ site suggests that it is a very axially distorted octahedron (where both axial bonds are 2.479(4) Å) that has four weaker equatorial bonds of 2.825(2) Å in length. $[(Li/Sn)S_6]$ is similar to the AgS_6 octahedron in synthetic pavonite, where they are both axially distorted. The axial and equatorial bonds for the AgS_6 octahedron are 2.741(6) Å and 2.917(2) Å, respectively.[7] Slab II is slightly more complicated in terms of mixed occupancy, as the five octahedra along the one-dimensional chain are either $[SnS_6]$, $[(Bi/Li)S_6]$, or $[(Bi/Sn)S_6]$. The Bi/Li site is split 87% to 13% in terms of occupancy, and the Bi/Sn site is split 61% to 39%. The unique bonds at the Bi/Li site (2.745(3) Å and 2.642(4) Å) are slightly shorter than the Bi/Sn site (2.780(3) Å and 2.665(3) Å), which is unsurprising considering that the former contains the significantly smaller lithium cation and the latter is mixed with two atoms of almost identical ionic radii. These bond lengths are comparable to established literature bond lengths for bismuth sulfide and tin sulfide, with the former ranging from 2.697(14) Å to 2.961(11) Å and the latter ranging from 2.622(3) Å to 2.6618(19) Å.

$NaSn_2Bi_5S_{10}$ is also an n = 5 pavonite, but there are several notable differences in the occupancies of the metal sites in both Slab I and Slab II of the structure. The $[M'S_6]$ octahedron in Slab I is actually a Sn/Bi site (84% and 16% respectively) and does not contain any monovalent alkali metals. $[(Sn/Bi)S_6]$ is also a distorted octahedron, but not to the same extent as the lithium analogue, as the axial bonds are 2.734(12) Å and the weaker equatorial bonds are 2.856(7) Å. The $[(Sn/Bi)S_6]$ octahedron is surrounded by two $[(Bi/Na)S_5]$ square pyramids, where the occupancies are 79% and 21% respectively. In Slab II, the different octahedra along the diagonal chains are either $[SnS_6]$ or two unique $[(Na/Bi)S_6]$ octahedra. The Sn−S bond lengths are comparable to similar bonds in the lithium pavonite structure with values of 2.866(7) Å and 2.917(15) Å, and the values of the Na/Bi bonds across all three sites range from 2.644(10) Å to 2.950(10) Å in length. In both structures, the bismuth- and tin-containing octahedra are distorted due to their stereoactive lone pairs ($6s^2$ for and $5s^2$ for bismuth and tin, respectively), which persists despite the presence of mixed occupancy with alkali metals at the sites.[29]

Optical Measurements and Electronic Structure Calculations. Both $LiSn_2Bi_5S_{10}$ and $NaSn_2Bi_5S_{10}$ are direct band gap semiconductors with values of 0.31(2) eV and 0.07(2) eV respectively. The fact that the band gap of the sodium analogue is significantly smaller occurs due to differences in mixed occupancy of the individual sites. Instead of sodium being primarily localized to the pseudo-octahedral geometry of Slab I in the structure, it is spread out relatively evenly across the bismuth sites in Slab II, significantly altering the band structure of the material relative to its analogue. The differences in site occupancy disorder for the two structures are corroborated by the band structures of both compounds, as DFT predicts a wider band gap for the lithium pavonite structure compared to its sodium counterpart (Figure 5).

The band structures for $LiSn_2Bi_5S_{10}$ and $NaSn_2Bi_5S_{10}$ are significantly different, as seen in Figure 5. The predicted band gap for $LiSn_2Bi_5S_{10}$ (0.25 eV) is in good agreement with the true band gap of 0.31(2) eV, but the predicted gap of the sodium analogue (0.15 eV) is actually higher than the true gap that is measured experimentally (0.07(2) eV), an anomalous

DOI: 10.1021/acs.inorgchem.7b03091
Inorg. Chem. 2018, 57, 2260−2268

result given the tendency of DFT to underestimate band gaps. The densities of states (DOS) for each structure were similar in that the valence band maximum (VBM) of both compounds is composed of Sn 5s and S 3p character, and the conduction band minimum (CBM) is almost entirely Bi 6p character with minimal contribution from Sn 5s orbitals. The alkali metal in both cases has a negligible effect on the density of states, as their highest occupied orbitals are not close enough in energy to contribute to the band edges. However, even though the alkali metals do not directly contribute to the density of states, their presence in each structure is important due to the differences in site occupancy disorder. Their differing ionic radii dictate which atoms they share occupancy with, and this in turn alters the individual DOS peaks for each atom listed, resulting in the vastly different band structures presented in Figure 5. The valence bands differ in that $LiSn_2Bi_5S_{10}$ has much broader bands, but $NaSn_2Bi_5S_{10}$ has much more dispersive bands. The opposite is true in the conduction bands of the two structures, as the conduction band is much more dispersive in $LiSn_2Bi_5S_{10}$ and broader in the sodium analogue.

Electrical and Thermal Measurements. Thermoelectric measurements were performed on $LiSn_2Bi_5S_{10}$ to determine its potential for this application (see Figure 6). Thermoelectric

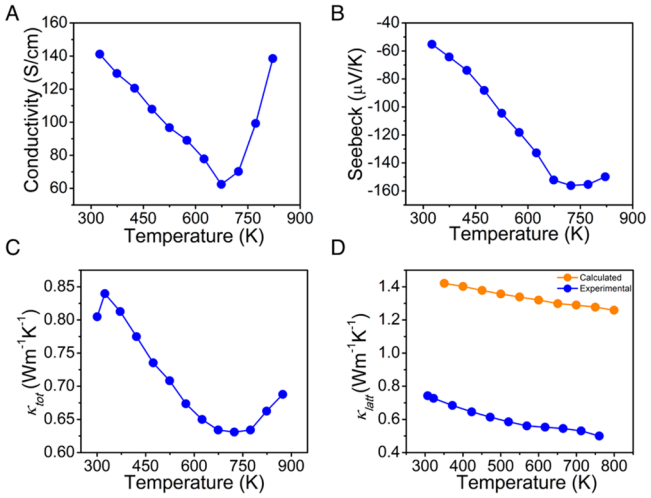

Figure 6. Thermoelectric property measurements for $LiSn_2Bi_5S_{10}$. Electrical conductivity (A), Seebeck coefficient (B), total thermal conductivity (C), and experimental and simulated lattice thermal conductivity (D).

materials and their efficiency are governed by the equation $ZT = \frac{\sigma S^2 T}{\kappa}$, where ZT is the dimensionless figure of merit, σ is the electrical conductivity, S is the Seebeck coefficient, T is absolute temperature, and κ is the total thermal conductivity (which has both lattice and electronic components). Most attempts to improve ZT values in thermoelectric materials have come from optimization of known, high symmetry materials through various methods such as doping,[30,31] nanostructuring,[32,33] and band convergence.[34,35] One other paradigm for pursuing high ZT thermoelectrics is the investigation of materials with complex crystal and electronic structures as well as large unit cells, such as ternary and quaternary chalcogenides with ultralow thermal conductivity.[36,37] Bismuth chalcogenides comprise a significant portion of all thermoelectric research, as $Bi_{2-x}Sb_xTe_3$ remains the prototypical example of a material that can be utilized near room temperature for practical applications.[38]

$LiSn_2Bi_5S_{10}$ behaves as a doped n-type semiconductor with a conductivity of around 165 S/cm at room temperature. It decreases with metal-like behavior until around 700 K, where the conductivity stops falling and then slightly increases due to bipolar diffusion. Hall effect measurements show a carrier concentration of approximately 1.2×10^{19} cm^{-3}, while the Seebeck coefficient starts at -55 μV/K, increases in magnitude to -160 μV/K, and undergoes a similar turnover at 700 K to the electrical conductivity, consistent with an increase in carrier concentration as a result of bipolar diffusion.

$LiSn_2Bi_5S_{10}$ has very low thermal conductivity (i.e., below 1 W m^{-1} K^{-1}) of 0.80 W m^{-1} K^{-1} at room temperature. The thermal conductivity decreases to a minimum of 0.625 W m^{-1} K^{-1} at 723 K, highlighting the intrinsically low thermal conductivity of this structure. The pavonite structure has been previously reported to have ultralow thermal conductivity for several different compounds due to its lower symmetry, complex crystal structure, and the presence of heavy elements such as bismuth.[14,26] However, the thermal conductivity of the $LiSn_2Bi_5S_{10}$ is comparable to that of synthetic pavonite ($AgBi_3S_5$) at room temperature (0.75 W m^{-1} K^{-1}) and lower at high temperatures, which is most likely attributable to the considerable site occupancy disorder and more complex composition of its structure compared to the original mineral.[14]

The theoretically simulated lattice thermal conductivity, using an ordered supercell of $LiSn_2Bi_5S_{10}$, is significantly higher than the actual experimental result. The higher lattice thermal conductivity is attributable to the quantitative limitations of DFT to accurately depict the amount of phonon scattering in a structure with as much disorder as $LiSn_2Bi_5S_{10}$. The higher value is also attributable to the fact that the experimental sample has a minor secondary phase of $n = 4$ pavonite, possibly helping to scatter phonons and lowering the experimental thermal conductivity. However, the qualitative trends are in good agreement, as the lattice thermal conductivities both decrease monotonically as a function of temperature in both the experimental and simulated cases. The lattice thermal conductivity in bismuth sulfide at room temperature is approximately 1.3 W m^{-1} K^{-1}, which is almost double that of $LiSn_2Bi_5S_{10}$ at the same temperature (0.743 W m^{-1} K^{-1}), supporting the claim that the lower symmetry and site occupancy disorder of the pavonite structure play a role in its ultralow thermal conductivity.[39] In addition, the distortive environment of the Sn and Bi atoms from the stereoactive lone-pair s^2 electrons and their pronounced repulsive interactions may also play a role in lowering the thermal conductivity of $LiSn_2Bi_5S_{10}$.[40]

The calculated phonon dispersion of $LiSn_2Bi_5S_{10}$ shows that the transverse acoustic phonon modes have slower velocities (and thus lower thermal conductivity along that path) than the longitudinal mode along all three axes (Figure 7). In the Brillouin zone, Γ to Z corresponds to the a direction, Γ to X corresponds to the b direction, and Γ to Y corresponds to the c direction. The transverse modes are similar in the c direction (through the layers), different in the a direction (between the layers), and comparably spaced in the b direction (stacking both slabs), with the red transverse mode being consistently lower in every direction. The Brillouin zone highlights the anisotropy of the pavonite structure type, as phonon transport is significantly different depending on the crystal direction. The phonon density of states shows that acoustic phonon transport

DOI: 10.1021/acs.inorgchem.7b03091
Inorg. Chem. 2018, 57, 2260−2268

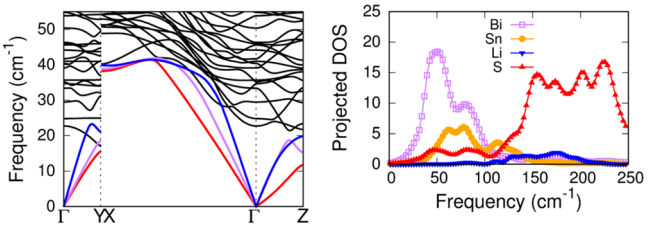

Figure 7. Phonon dispersion (left) and phonon density of states (right) of $LiSn_2Bi_5S_{10}$. The red and purple lines in the phonon dispersion graph correspond to the transverse acoustic phonon modes, and the blue lines correspond to the longitudinal acoustic phonon modes. The black lines are optical modes.

in this material is primarily based on the motions of the heavier bismuth atoms with minimal contribution from tin. The phonon dispersion calculations are consistent with the intrinsically low thermal conductivity of the structure as well as its anisotropic nature.

CONCLUSIONS

The crystal structures of $LiSn_2Bi_5S_{10}$ and $NaSn_2Bi_5S_{10}$ display considerable site occupancy disorder of the alkali metal on both Bi and Sn sites, and their differences in site occupancy disorder significantly alter their band structures and their optical properties. The thermal conductivity of $LiSn_2Bi_5S_{10}$ is ultralow due to the intrinsic attributes of the pavonite structure as well as its complex composition and site occupancy disorder. Phonon dispersion calculations highlight the anisotropic nature of the structure, as the transverse acoustic phonon modes do not facilitate phonon transport as easily as the longitudinal acoustic phonon mode. The lattice contribution to thermal conductivity should increase as the *n*-member in the homologous series increases, as the structure would become more and more isotropic and the symmetry of the structure would trend toward a defect rock-salt such as Bi_2S_3. The pavonite structure is a promising host candidate for thermoelectric investigation, as these materials inherently have low thermal conductivity and narrow band gaps. There is also a considerable phase space to explore, as the respective homologous series could lead to high performing thermoelectric materials as well as materials with tunable electronic properties.

ASSOCIATED CONTENT

Supporting Information

The Supporting Information is available free of charge on the ACS Publications website at DOI: 10.1021/acs.inorgchem.7b03091.

Additional experimental details, crystallographic tables, PXRDs, SEM-EDS, ICP-OES, and thermoelectric property measurements (PDF)

Accession Codes

CCDC 1811757−1811758 contain the supplementary crystallographic data for this paper. These data can be obtained free of charge via www.ccdc.cam.ac.uk/data_request/cif, or by emailing data_request@ccdc.cam.ac.uk, or by contacting The Cambridge Crystallographic Data Centre, 12 Union Road, Cambridge CB2 1EZ, UK; fax: +44 1223 336033.

AUTHOR INFORMATION

Corresponding Author

*E-mail: m-kanatzidis@northwestern.edu.

ORCID

Jason F. Khoury: 0000-0003-4769-6730
Constantinos C. Stoumpos: 0000-0001-8396-9578
Chris Wolverton: 0000-0003-2248-474X
Mercouri G. Kanatzidis: 0000-0003-2037-4168

Notes

The authors declare no competing financial interest.

ACKNOWLEDGMENTS

This work was supported by the National Science Foundation Grant DMR-1708254, as well as the NASA Science Mission Directorate's Radioisotope Power Systems Thermoelectric Technology Development. S.H. and C.W. (DFT calculations) were supported by the Department of Energy, Office of Science Basic Energy Sciences Grant DE-SC0014520. C.D.M. was supported by IMSERC at Northwestern University, which has received support from the Soft and Hybrid Nanotechnology Experimental (SHyNE) Resource (NSF NNCI-1542205); the State of Illinois; and International Institute for Nanotechnology (IIN). We acknowledge the use of QUEST, the supercomputer resource facility at Northwestern University. We thank Michael L. Aubrey for helpful discussions, and Daniel G. Chica for assisting in ammonia synthesis of Na_2S and Li_2S.

REFERENCES

(1) Sootsman, J. R.; Chung, D. Y.; Kanatzidis, M. G. New and Old Concepts in Thermoelectric Materials. *Angew. Chem., Int. Ed.* **2009**, *48*, 8616−8639.

(2) Malliakas, C. D.; Chung, D. Y.; Claus, H.; Kanatzidis, M. G. Superconductivity in the Narrow Gap Semiconductor $RbBi_{11/3}Te_6$. *J. Am. Chem. Soc.* **2016**, *138*, 14694−14698.

(3) Chung, D.-Y.; Iordanidis, L.; Rangan, K. K.; Brazis, P. W.; Kannewurf, C. R.; Kanatzidis, M. G. First Quaternary A−Pb−Bi−Q (A = K, Rb, Cs; Q = S, Se) Compounds: Synthesis, Structure, and Properties of α- and β-$CsPbBi_3Se_6$, $APbBi_3Se_6$, (A = K, Rb), and $APbBi_3S_6$ (A = Rb, Cs). *Chem. Mater.* **1999**, *11*, 1352−1362.

(4) Mrotzek, A.; Kanatzidis, M. G. Design" in Solid-State Chemistry Based on Phase Homologies. The Concept of Structural Evolution and the New Megaseries $A_m[M_{1+l}Se_{2+l}]_{2m}[M_{2l+n}Se_{2+3l+n}]$. *Acc. Chem. Res.* **2003**, *36*, 111−119.

(5) Iordanidis, L.; Schindler, J. L.; Kannewurf, C. R.; Kanatzidis, M. G. $ALn_{1\pm x}Bi_{4\pm x}S_8$ (A = K,Rb;Ln = La,Ce,Pr,Nd): New Semiconducting Quaternary Bismuth Sulfides. *J. Solid State Chem.* **1999**, *143*, 151−162.

(6) Kanatzidis, M. G. Discovery-Synthesis, Design, and Prediction of Chalcogenide Phases. *Inorg. Chem.* **2017**, *56*, 3158−3173.

(7) Makovicky, E.; Mumme, W. G.; Watts, J. A. The crystal structure of synthetic pavonite, $AgBi_3S_5$, and the definition of the pavonite homologous series. *Can. Mineral* **1977**, *15*, 339−348.

(8) Izumino, Y.; Nakashima, K.; Nagashima, M. Makovickyite and cupromakovickyite from the Obari mine, Yamagata Prefecture, Japan. *J. Mineral. Petrol. Sci.* **2013**, *108*, 94−100.

(9) Nakhal, S.; Wiedemann, D.; Stanje, B.; Dolotko, O.; Wilkening, M.; Lerch, M. $LiBi_3S_5$—A lithium bismuth sulfide with strong cation disorder. *J. Solid State Chem.* **2016**, *238*, 60−67.

(10) Agha, E. C.; Malliakas, C. D.; Im, J.; Jin, H.; Zhao, L.-D.; Freeman, A. J.; Kanatzidis, M. G. $LiPbSb_3S_6$: A Semiconducting Sulfosalt with Very Low Thermal Conductivity. *Inorg. Chem.* **2014**, *53*, 673−675.

(11) Chung, D.-Y.; Choi, K.-S.; Iordanidis, L.; Schindler, J. L.; Brazis, P. W.; Kannewurf, C. R.; Chen, B.; Hu, S.; Uher, C.; Kanatzidis, M. G. High Thermopower and Low Thermal Conductivity in Semiconducting Ternary K−Bi−Se Compounds. Synthesis and Properties

DOI: 10.1021/acs.inorgchem.7b03091
Inorg. Chem. 2018, 57, 2260−2268

of β-$K_2Bi_8Se_{13}$ and $K_{2.5}Bi_{8.5}Se_{14}$ and Their Sb Analogues. *Chem. Mater.* **1997**, *9*, 3060−3071.
(12) Olvera, A.; Shi, G.; Djieutedjeu, H.; Page, A.; Uher, C.; Kioupakis, E.; Poudeu, P. F. P. $Pb_7Bi_4Se_{13}$: A Lillianite Homologue with Promising Thermoelectric Properties. *Inorg. Chem.* **2015**, *54*, 746−755.
(13) Casamento, J.; Lopez, J. S.; Moroz, N. A.; Olvera, A.; Djieutedjeu, H.; Page, A.; Uher, C.; Poudeu, P. F. P. Crystal Structure and Thermoelectric Properties of the ^{7,7}L Lillianite Homologue $Pb_6Bi_2Se_9$. *Inorg. Chem.* **2017**, *56*, 261−268.
(14) Kim, J.-H.; Chung, D.-Y.; Bilc, D.; Loo, S.; Short, J.; Mahanti, S. D.; Hogan, T.; Kanatzidis, M. G. Crystal Growth, Thermoelectric Properties, and Electronic Structure of $AgBi_3S_5$ and $AgSb_xBi_{3-x}S_5$ (x = 0.3). *Chem. Mater.* **2005**, *17*, 3606−3614.
(15) Tan, G.; Hao, S.; Zhao, J.; Wolverton, C.; Kanatzidis, M. G. High Thermoelectric Performance in Electron-doped $AgBi_3S_5$ with Ultralow Thermal Conductivity. *J. Am. Chem. Soc.* **2017**, *139*, 6467−6473.
(16) Lin, H.; Tan, G.; Shen, J.-N.; Hao, S.; Wu, L.-M.; Calta, N.; Malliakas, C.; Wang, S.; Uher, C.; Wolverton, C.; Kanatzidis, M. G. Concerted Rattling in $CsAg_5Te_3$ Leading to Ultralow Thermal Conductivity and High Thermoelectric Performance. *Angew. Chem., Int. Ed.* **2016**, *55*, 11431−11436.
(17) STOE & Cie, X-area (version 1.18) and X-red32 (version 1.04). 2002.
(18) Sheldrick, G. A short history of SHELX. *Acta Crystallogr., Sect. A: Found. Crystallogr.* **2008**, *64*, 112−122.
(19) Zhao, J.; Islam, S. M.; Tan, G.; Hao, S.; Wolverton, C.; Li, R. K.; Kanatzidis, M. G. The New Semiconductor $Cs_4Cu_3Bi_9S_{17}$. *Chem. Mater.* **2017**, *29* (4), 1744−1751.
(20) Perdew, J. P.; Burke, K.; Ernzerhof, M. Generalized Gradient Approximation Made Simple. *Phys. Rev. Lett.* **1996**, *77*, 3865−3868.
(21) Kresse, G.; Furthmüller, J. Efficient iterative schemes for ab initio total-energy calculations using a plane-wave basis set. *Phys. Rev. B: Condens. Matter Mater. Phys.* **1996**, *54* (16), 11169−11186.
(22) Li, Q.; Yao, Z.; Wu, J.; Mitra, S.; Hao, S.; Sahu, T. S.; Li, Y.; Wolverton, C.; Dravid, V. P. Intermediate phases in sodium intercalation into MoS_2 nanosheets and their implications for sodium-ion batteries. *Nano Energy* **2017**, *38*, 342−349.
(23) Asen-Palmer, M.; Bartkowski, K.; Gmelin, E.; Cardona, M.; Zhernov, A. P.; Inyushkin, A. V.; Taldenkov, A.; Ozhogin, V. I.; Itoh, K. M.; Haller, E. E. Thermal conductivity of germanium crystals with different isotopic compositions. *Phys. Rev. B: Condens. Matter Mater. Phys.* **1997**, *56*, 9431−9447.
(24) Morelli, D. T.; Heremans, J. P.; Slack, G. A. Estimation of the isotope effect on the lattice thermal conductivity of group IV and group III-V semiconductors. *Phys. Rev. B: Condens. Matter Mater. Phys.* **2002**, *66*, 195304.
(25) Borup, K. A.; de Boor, J.; Wang, H.; Drymiotis, F.; Gascoin, F.; Shi, X.; Chen, L.; Fedorov, M. I.; Muller, E.; Iversen, B. B.; Snyder, G. J. Measuring thermoelectric transport properties of materials. *Energy Environ. Sci.* **2015**, *8*, 423−435.
(26) Hwang, J.-Y.; Ahn, J. Y.; Lee, K. H.; Kim, S. W. Structural optimization for thermoelectric properties in Cu-Bi-S pavonite compounds. *J. Alloys Compd.* **2017**, *704*, 282−288.
(27) Gospodinov, G. G.; Odin, I. N.; Popovkin, B. A.; Novoselova, A. V. The system SnS - Bi2S3. *Inorg. Mater.* **1971**, *7*, 441−442.
(28) Takeuchi, Y.; Takagi, J.; Yamanaka, T. Structural characterization of the high-temperature phase V on the PbS−Bi_2S_3 join. *Z. Kristallogr. - Cryst. Mater.* **1974**, *140*, 249−272.
(29) Kanatzidis, M. G.; McCarthy, T. J.; Tanzer, T. A.; Chen, L.-H.; Iordanidis, L.; Hogan, T.; Kannewurf, C. R.; Uher, C.; Chen, B. Synthesis and Thermoelectric Properties of the New Ternary Bismuth Sulfides $KBi_{6.33}S_{10}$ and $K_2Bi_8S_{13}$. *Chem. Mater.* **1996**, *8*, 1465−1474.
(30) Snyder, G. J.; Toberer, E. S. Complex thermoelectric materials. *Nat. Mater.* **2008**, *7*, 105−114.
(31) Zeier, W. G.; Zevalkink, A.; Gibbs, Z. M.; Hautier, G.; Kanatzidis, M. G.; Snyder, G. J. Thinking Like a Chemist: Intuition in Thermoelectric Materials. *Angew. Chem., Int. Ed.* **2016**, *55*, 6826−6841.
(32) Biswas, K.; He, J.; Blum, I. D.; Wu, C.-I.; Hogan, T. P.; Seidman, D. N.; Dravid, V. P.; Kanatzidis, M. G. High-performance bulk thermoelectrics with all-scale hierarchical architectures. *Nature* **2012**, *489*, 414−418.
(33) Poudel, B.; Hao, Q.; Ma, Y.; Lan, Y.; Minnich, A.; Yu, B.; Yan, X.; Wang, D.; Muto, A.; Vashaee, D.; Chen, X.; Liu, J.; Dresselhaus, M. S.; Chen, G.; Ren, Z. High-Thermoelectric Performance of Nanostructured Bismuth Antimony Telluride Bulk Alloys. *Science* **2008**, *320*, 634−638.
(34) Pei, Y.; Shi, X.; LaLonde, A.; Wang, H.; Chen, L.; Snyder, G. J. Convergence of electronic bands for high performance bulk thermoelectrics. *Nature* **2011**, *473*, 66−69.
(35) Pei, Y.; Chang, C.; Wang, Z.; Yin, M.; Wu, M.; Tan, G.; Wu, H.; Chen, Y.; Zheng, L.; Gong, S.; Zhu, T.; Zhao, X.; Huang, L.; He, J.; Kanatzidis, M. G.; Zhao, L.-D. Multiple Converged Conduction Bands in $K_2Bi_8Se_{13}$: A Promising Thermoelectric Material with Extremely Low Thermal Conductivity. *J. Am. Chem. Soc.* **2016**, *138*, 16364−16371.
(36) Chung, D.-Y.; Hogan, T.; Brazis, P.; Rocci-Lane, M.; Kannewurf, C.; Bastea, M.; Uher, C.; Kanatzidis, M. G. $CsBi_4Te_6$: A High-Performance Thermoelectric Material for Low-Temperature Applications. *Science* **2000**, *287*, 1024−1027.
(37) Chung, D.-Y.; Hogan, T. P.; Rocci-Lane, M.; Brazis, P.; Ireland, J. R.; Kannewurf, C. R.; Bastea, M.; Uher, C.; Kanatzidis, M. G. A New Thermoelectric Material: $CsBi_4Te_6$. *J. Am. Chem. Soc.* **2004**, *126*, 6414−6428.
(38) Tan, G.; Zhao, L.-D.; Kanatzidis, M. G. Rationally Designing High-Performance Bulk Thermoelectric Materials. *Chem. Rev.* **2016**, *116*, 12123−12149.
(39) Biswas, K.; Zhao, L.-D.; Kanatzidis, M. G. Tellurium-Free Thermoelectric: The Anisotropic n-Type Semiconductor Bi_2S_3. *Adv. Energy Mater.* **2012**, *2*, 634−638.
(40) Dong, Y.; Khabibullin, A. R.; Wei, K.; Salvador, J. R.; Nolas, G. S.; Woods, L. M. Bournonite $PbCuSbS_3$: Stereochemically Active Lone-Pair Electrons that Induce Low Thermal Conductivity. *ChemPhysChem* **2015**, *16*, 3264−3270.

DOI: 10.1021/acs.inorgchem.7b03091
Inorg. Chem. 2018, 57, 2260−2268